

Exciton tuning in monolayer WSe₂ via substrate induced electron doping

Yang Pan^{1,2*}, Mahfujur Rahaman³, Lu He^{1,2}, Ilya Milekhin^{1,2}, Gopinath Manoharan⁴, Muhammad Awais Aslam⁵, Thomas Blaudeck^{2,4,6}, Andreas Willert⁶, Aleksandar Matković⁵, Teresa I. Madeira^{1,2}, and Dietrich R. T. Zahn^{1,2}

¹Semiconductor Physics, Institute of Physics, Chemnitz University of Technology, Chemnitz, Germany

²Center for Materials, Architectures, and Integration of Nanomembranes (MAIN), Chemnitz University of Technology, Chemnitz, Germany

³Department of Electrical and Systems Engineering, University of Pennsylvania, Philadelphia, PA, USA

⁴Center for Microtechnologies, Chemnitz University of Technology, Chemnitz, Germany

⁵Institute of Physics, Montanuniversität Leoben, Leoben, Austria

⁶Fraunhofer Institute for Electronic Nano Systems, Chemnitz, Germany

*Corresponding author: yang.pan@physik.tu-chemnitz.de

Abstract

We report on large exciton tuning in WSe₂ monolayers via substrate induced non-degenerate doping. We observe a redshift of ~ 62 meV for the *A* exciton together with a 1-2 orders of magnitude photoluminescence (PL) quenching when the monolayer WSe₂ is brought in contact with highly oriented pyrolytic graphite (HOPG) compared to the dielectric substrates such as hBN and SiO₂. As the evidence of doping from HOPG to WSe₂, a drastic increase of the trion emission intensity was observed. Using a systematic PL and Kelvin probe force microscopy (KPFM) investigation on WSe₂/HOPG, WSe₂/hBN, and WSe₂/graphene, we conclude that this unique excitonic behavior is induced by electron doping from the substrate. Our results propose a simple yet efficient way for exciton tuning in monolayer WSe₂, which plays a central role in the fundamental understanding and further device development.

1 Introduction

Beyond graphene [1], transition metal dichalcogenides (TMDCs) are currently at the center of 2D materials research, owing to their extraordinary optical, electrical, thermal, mechanical properties [2–5], and, most importantly, to the unique indirect- to direct-bandgap transition when the material is thinned from bulk to monolayer [6, 7]. Different approaches of exciton tuning and bandgap engineering have been reported such as changing the dielectric environment, mechanical straining, doping, alloying, injecting plasmonic hot electrons, and manipulating the carrier concentration via external electric field [8–15].

In this work, we report on tuning the exciton energy in monolayer WSe₂ via substrate induced non-degenerate electron doping. We observe a ~ 62 meV redshift of the monolayer WSe₂ *A* excitonic emission (from ~ 1.65 eV to ~ 1.71 eV) together with a few orders of magnitude photoluminescence (PL) quenching when the material is brought in contact with HOPG compared to the WSe₂ excitonic feature on dielectric substrates such as hBN, SiO₂, and polydimethylsiloxane (PDMS), which has been measured and reported in our previous work [16]. As a by-product, a drastic increase of the trion emission intensity up to 5.5 times was observed, which is a characteristic of electron doping in TMDC monolayers. To understand this unique behavior, we employed a systematic PL and Kelvin probe force microscopy (KPFM) investigation on different TMDC/substrate combinations, namely WSe₂/HOPG, WSe₂/graphene, and WSe₂/hBN as a reference. Surprisingly, we were only able to observe such pronounced redshift when WSe₂ is in contact with HOPG but not with graphene. The KPFM measurements provide different contact potential difference (CPD)

values when comparing WSe₂/HOPG to WSe₂/graphene and WSe₂/hBN. This indicates different Fermi level positions and different carrier concentrations in WSe₂. The PL quenching, redshift, increase of trion emission intensity, and different CPD values all conclusively point towards electrons from the HOPG substrate injected to WSe₂ and leading to bandgap renormalization and thus the tuning of exciton energy. Our work explains the unique behavior of monolayer WSe₂/HOPG and demonstrates a simple yet efficient method, which enables to tune the exciton energy in monolayer WSe₂ by ~ 62 meV. This is essential for fundamental studies and the development of devices such as photodetectors, excitonic LEDs, and the coupling with plasmonics [17–20].

2 Materials and methods

2.1 Sample preparation

Few layer hBN (from 2D semiconductors), graphene (from NGS Naturgraphit), and monolayer WSe₂ (from HQ graphene) are mechanically exfoliated from their bulk crystals via Nitto tape onto a PDMS stamp and then transferred bottom-to-top onto the HOPG substrate following a deterministic all-dry transfer technique [21, 22]. All materials on PDMS are first characterized by PL and Raman prior to transfer. HOPG was cleaved before transfer to ensure a fresh surface. After transfer, the samples are annealed in a nitrogen atmosphere at 150 °C for 2 hours to optimize the contact between flakes and ensure a clean surface. The detailed process used for sample fabrication is shown in Figs. 1S and 2S.

2.2 Optical spectroscopy

PL measurements are performed using a Horiba Xplora Plus equipped with a 100x, 0.9 NA objective, a spectrometer comprising 600 l/mm grating, and an electron-multiplying CCD (EMCCD). A DPSS 532 nm CW laser source was used for excitation. The laser power is ~ 100 μ W measured under the objective for PL measurements if not specified differently. The setup is equipped with a Märzhäuser motorized *xyz* stage with a 100 nm step size precision for PL mapping.

Raman spectra are acquired by a Horiba LabRAM HR spectrometer with a 100x, 0.9 NA objective, 2400 l/mm grating, and a liquid nitrogen cooled Symphony CCD detector. A solid-state 514.7 nm laser is used for excitation with a laser power ~ 100 μ W measured under the objective. We choose a confocal pinhole of 50 μ m to reach a high spectral resolution of approximately 0.8 cm^{-1} .

2.3 Kelvin probe force microscope

We use an AIST-NT SmartSPMTM 1000 for KPFM measurements. The KPFM measurements are performed in ambient condition with constant temperature and humidity. The NSG10 Pt coated tip is commercially available with a typical tip radius of ~ 35 nm.

3 Results and discussion

Figs. 1(a) and (b) display the optical microscope image and the schematic cross section of a WSe₂/hBN/HOPG hetero-stack, respectively. The monolayer WSe₂ is transferred onto the hBN/HOPG hetero-stack in a way that it creates contacts with both few layer hBN and HOPG. According to the atomic force microscopy (AFM) measurement shown in Fig. 4S, the top brown-colored hBN has a thickness of ~ 38.2 nm, and the middle part has a thickness of ~ 3.8 nm. We acquired a micro PL map on the sample with a step size of 0.5 μ m. As shown in the intensity map in Fig. 1(c), the PL intensity of WSe₂ on thick hBN is higher than that on thin hBN because of interference enhancement [23, 24]. More importantly, comparing the PL intensity of WSe₂ on hBN and HOPG, one can clearly identify that a drastic decrease of PL intensity occurs on HOPG. The few dots that still remain intense may correspond to bubbles or hydrocarbon contaminations at the interface, which can enhance the PL signal [25–27]. Fig. 1(d) displays the peak position map indicating that the sample is clearly divided into two parts: WSe₂/hBN with a peak position of ~ 1.65 eV and WSe₂/HOPG with a peak position of ~ 1.55 eV.

The detailed spectra of WSe₂/hBN and WSe₂/HOPG are shown in Fig. 1(e). A strong PL quenching of 1-2 orders of magnitude is observed when WSe₂ is in contact with HOPG, which indicates charge dissociation through the junction or charge transfer between WSe₂ and HOPG [24, 28]. Monolayer WSe₂ on hBN shows a characteristic PL at ~ 1.65 eV, which is consistent with the literature values [16, 29], while the PL peak position of WSe₂/HOPG shows a marked

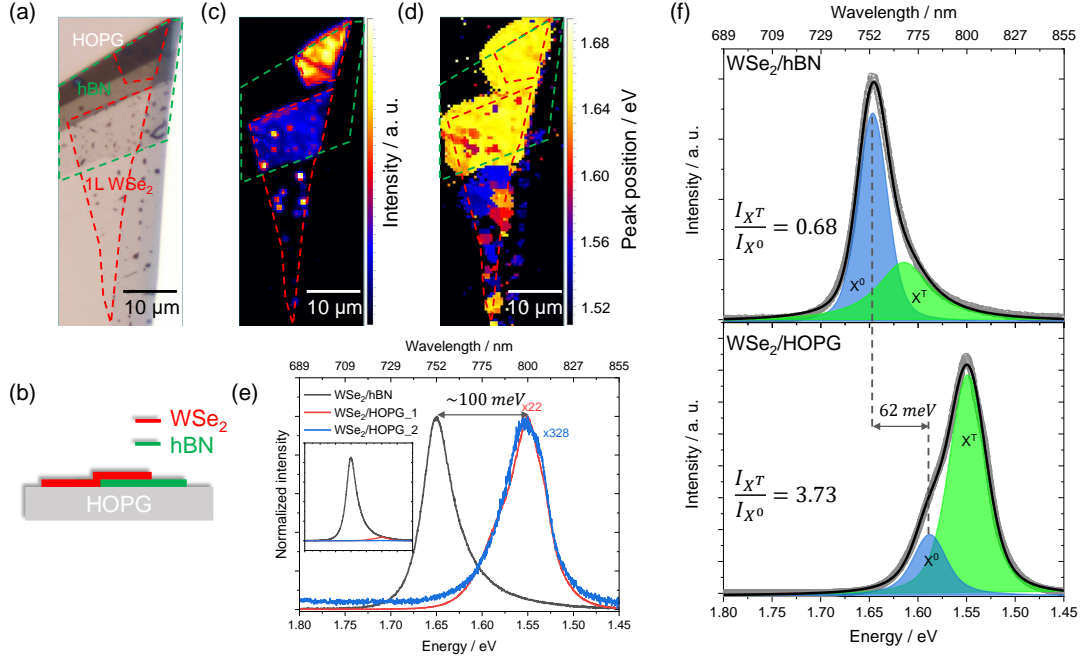


Figure 1: (a) optical microscope image and (b) schematic cross section of the WSe₂/hBN/HOPG hetero-stack. PL (c) intensity and (d) peak position map of the sample. (e) PL spectra of WSe₂/hBN and WSe₂/HOPG. For comparison, the PL intensity of WSe₂/HOPG is normalized to that of WSe₂/hBN. Inset: as-measured (not-normalized) PL spectra. (f) Fitted PL spectra of WSe₂/hBN and WSe₂/HOPG.

~ 100 meV redshift, which is much higher than the reported value caused by changing of dielectric environment [8]. Besides the quenching and redshift, the PL line shape changes significantly. We thus decomposed the PL spectra into peaks corresponding to the radiative recombination of different exciton/trion species in monolayer WSe₂. As shown in Fig. 1(f), two peaks with a Voigt line shape were identified in the fitted spectra. The neutral exciton (X^0) originates from the direct bandgap transition at the K point in the Brillouin zone and there is a charged exciton peak also known as trion X^T [29–32]. We also investigated the Stokes shift of monolayer WSe₂ as shown in Fig. 3S, which is negligible with value of ~ 2 meV. It is therefore fair enough to consider the PL peak position as the exciton energy. The fitting result suggests a 62 meV redshift of X^0 and most interestingly, a drastic increase of the relative X^T intensity. The ratio of I_{X^T}/I_{X^0} increases from 0.68 on hBN to 3.73 on HOPG, which is a strong evidence of higher electron concentration in WSe₂ on HOPG than in WSe₂ on hBN.

Even though we propose that charge transfer and electron doping from HOPG to monolayer WSe₂ seem to be the most reasonable mechanism of PL quenching, redshift, and increasing trion emission intensity, we still carefully examined that they do not originate from the defect-bound localized states or strain due to lattice mismatch. Power dependent PL intensities of WSe₂/hBN and WSe₂/HOPG are displayed in Fig. 2(a). The PL intensity is obtained from the integrated area of the Voigt fitted X^0 and X^T features. The PL intensity as a function of excitation laser power is then fitted by a power law: $I \propto P^\alpha$ [29, 33], where the extracted exponential factor $\alpha_{X^0 \text{ WSe}_2/\text{hBN}} = 0.75 \pm 0.02$, $\alpha_{X^T \text{ WSe}_2/\text{hBN}} = 0.80 \pm 0.01$, $\alpha_{X^0 \text{ WSe}_2/\text{HOPG}} = 0.89 \pm 0.03$, and $\alpha_{X^T \text{ WSe}_2/\text{HOPG}} = 0.89 \pm 0.05$ for X^0 and X^T on WSe₂/hBN and WSe₂/HOPG, respectively. The fitting results suggest a sublinear power dependence of the PL intensity for both X^0 and X^T on WSe₂/hBN and WSe₂/HOPG and do not show any saturation phenomena at high laser power, which excludes the possibility of defects as the origin of the observed behavior [34]. Fig. 2(b) shows the high spectral resolution ($\sim 0.8 \text{ cm}^{-1}$) Raman spectra of WSe₂/hBN and WSe₂/HOPG. The most intense peak at $\sim 250 \text{ cm}^{-1}$ corresponds to the combination of the in-plane E_{2g} and out-of-plane A_{1g} vibrational modes, which are almost degenerate at the same frequency [16, 35–37]. The feature at $\sim 260 \text{ cm}^{-1}$ is a second order peak caused by a double resonance effect involving the longitudinal acoustic phonon at the M point in the Brillouin zone assigned as 2LA(M) [37, 38]. The E_{2g}/A_{1g} mode is highly sensitive to the strain [39, 40]. The fitted Raman spectra reveal a small 0.15 cm^{-1} peak position difference, which indicates that strain is also small and cannot account for the huge

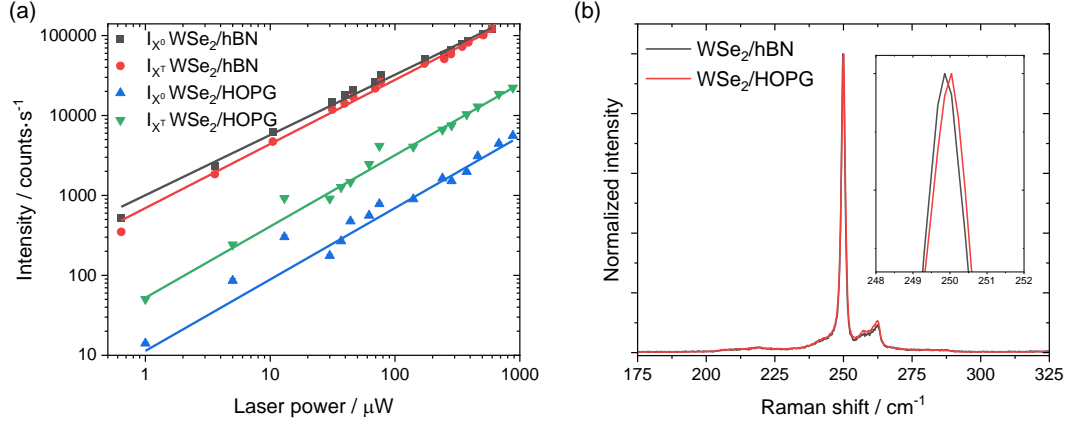


Figure 2: (a) PL intensity as a function of excitation power for X^0 and X^T emissions from WSe_2/hBN and WSe_2/HOPG . Solid lines are fits to a power law: $I \propto P^\alpha$. (b) High spectral resolution Raman spectra of WSe_2/hBN and WSe_2/HOPG . Inset is a zoom in at $248\text{--}252\text{ cm}^{-1}$.

redshift in PL.

KPFM is a powerful technique to obtain local surface potential and Fermi level position in the nanoscale [24, 41]. We therefore measured KPFM on the $\text{WSe}_2/\text{hBN}/\text{HOPG}$ hetero-stack to obtain further insight in the energy level alignment at the various interfaces. In the ideal case KPFM measures the contact potential difference (CPD) between the metallic AFM tip and the sample according to the relation: $\text{CPD} = (\phi_{\text{sample}} - \phi_{\text{tip}})/e$, where ϕ_{sample} and ϕ_{tip} are the work functions of the sample and the tip, and e is the elementary charge. KPFM does not give a quantitative, absolute value of the Fermi level position in ambient conditions, because the CPD value is known to be strongly influenced by the measurement environment, tip geometry, parasitic effects such as capacitive coupling, as well as the chosen experimental parameters [42–45]. Nevertheless, it still qualitatively indicates the trend of Fermi level position and material work functions [24, 41, 46, 47]. The values of the energy levels discussed in the following paragraph are directly extracted from the KPFM measurements.

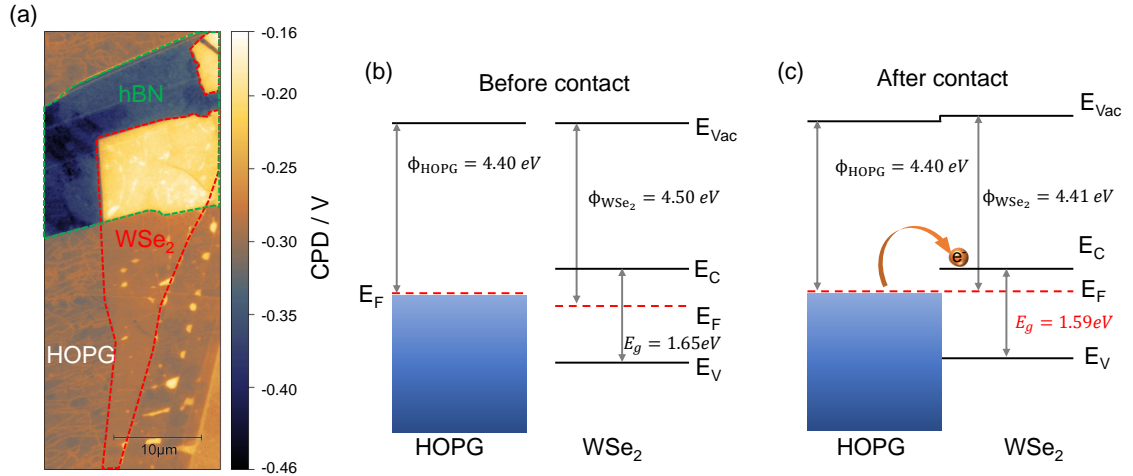


Figure 3: (a) KPFM of $\text{WSe}_2/\text{hBN}/\text{HOPG}$. Band diagram of monolayer WSe_2 and HOPG before (b) and after (c) contact. Before contact means when WSe_2 is isolated from HOPG by hBN and after contact means that WSe_2 is on HOPG.

Fig. 3(a) shows the CPD map of $\text{WSe}_2/\text{hBN}/\text{HOPG}$. Even though it is the same monolayer WSe_2 flake, one can clearly distinguish the high contrast between WSe_2 on hBN and WSe_2 on HOPG. The absolute work function of HOPG is determined to be $\phi_{\text{HOPG}} = 4.4\text{ eV}$ by an ultra-violet photoelectron spectroscopy (UPS) measurement shown in Fig. 6S. The electron affinity of monolayer WSe_2 is reported to be $3.7\text{--}3.9\text{ eV}$ [48, 49]. We therefore calculate and draw the band diagrams of WSe_2 before (on hBN) and after (on HOPG) contacting with HOPG in Figs. 3(b) and (c), respectively. The band diagrams reveal a decrease of the work function or increase of

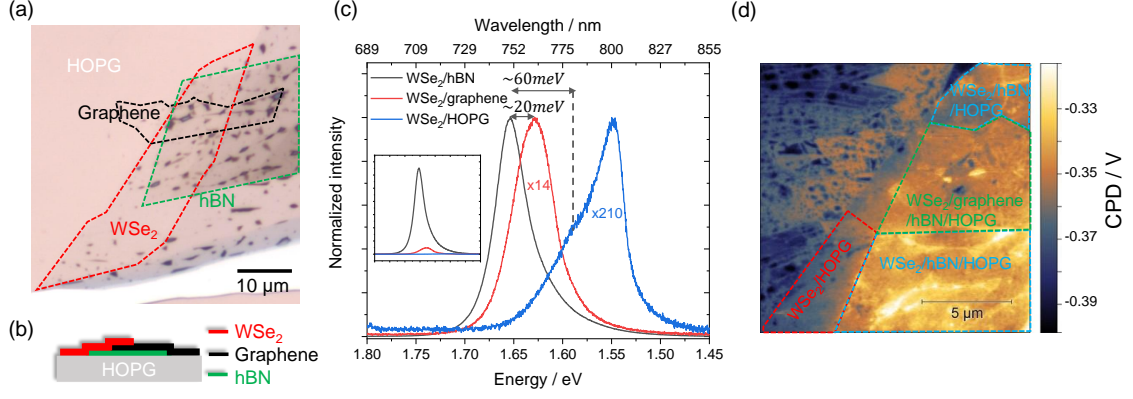


Figure 4: (a) optical microscope image and (b) schematic cross section of WSe₂/graphene/hBN/HOPG hetero-stack. (c) PL spectra of WSe₂/hBN, WSe₂/graphene, and WSe₂/HOPG. For comparison, the intensities of the WSe₂/graphene and WSe₂/HOPG PL are normalized to that of WSe₂/hBN/HOPG. Inset: as-measured (not-normalized) PL spectra. (d) KPFM of WSe₂/graphene/hBN/HOPG.

Fermi level when WSe₂ is in contact with HOPG, which indicates higher electron concentration in WSe₂ on HOPG than in WSe₂ on hBN. The high electron concentration in WSe₂/HOPG can only originate from electron doping from HOPG to WSe₂, which explains the PL quenching, redshift, and increasing trion emission intensity shown in Fig. 1.

Apparently interfacing WSe₂ with HOPG results in an efficient tuning of the exciton emission in a straightforward manner. Researchers also studied the combination of WSe₂ and graphene [8], yet did not report similar results. This naturally leads to the question: do graphene and graphite lead to a different interaction when interfaced with WSe₂? To answer this question, we prepared a hetero-stack of WSe₂/graphene/hBN/HOPG as shown in Figs. 4(a) and (b), where WSe₂ is partially on hBN, partially on graphene, and partially on HOPG. The PL spectra of WSe₂/hBN, WSe₂/graphene, and WSe₂/HOPG are shown in Fig. 4(c). Again, we observe similar PL quenching, redshift, and increasing trion emission intensity for WSe₂ on HOPG. However, a redshift of only 20 meV is detected on WSe₂/graphene, which is in excellent agreement with the value reported by Raja *et al.* [8]. This redshift of the *A* exciton is attributed to the altered local dielectric screening of the Coulomb interaction in WSe₂. A higher trion emission intensity is also not observed in the case of WSe₂/graphene. This clearly indicates that the interaction for WSe₂ on graphene is different from that for WSe₂ on HOPG. We assume that this difference is due to the lower amount of free electrons in graphene than that in HOPG. The KPFM measurement performed on such a sample is displayed in Fig. 4(d). A CPD contrast is only observed between WSe₂/HOPG and WSe₂/hBN with a value of $\Delta CPD_{WSe_2/hBN-WSe_2/HOPG} = (20.4 \pm 4.9) mV$, while WSe₂/graphene and WSe₂/hBN reveal a negligible difference of $\Delta CPD_{WSe_2/hBN-WSe_2/gr} = (2.4 \pm 4.3) mV$. This suggests that a significant change of the Fermi level position occurs due to electron doping from the substrate and only happens for WSe₂ on HOPG but not for WSe₂ on graphene.

4 Conclusions

In summary, we investigated WSe₂/hBN, WSe₂/graphene, and WSe₂/HOPG hetero-stacks. We observed a strong PL intensity quenching, 62 meV redshift of the *A* exciton, and a drastic increase of the trion emission intensity on WSe₂/HOPG compared to WSe₂/graphene and WSe₂/hBN. The KPFM results reveal a high CPD contrast, which indicates a renormalization of the energy level alignment at the interface. The effects observed for WSe₂ on HOPG are thus assigned to significant electron doping of the WSe₂ monolayer from the HOPG substrate. We propose a simple yet efficient way to tune the exciton emission in monolayer WSe₂ by substrate induced electron doping.

5 Acknowledgments

The authors gratefully acknowledge financial support by the Deutsche Forschungsgemeinschaft (DFG, projects ZA 146/43-1 and ZA 146/47-1). M.A.A. and A.M. acknowledge financial support by the Austrian Science Fund (FWF) under the grant no. I4323-N36. We thank Manuel Monecke for helping the UPS measurement.

6 Author contributions

Y.P. fabricated the samples, performed the measurements and analyzed the data. M.R., I.M. L.H., and T.I.M. contributed to data analysis and discussion. G.M., T.B. and A.W. performed the reflectance contrast measurement. M.A.A. and A.M. provided the graphene. D.R.T.Z. supervised the work. M.R. and D.R.T.Z. were involved in the evaluation and interpretation of the results. Y.P. wrote the manuscript. All authors discussed the results and commented on the manuscript.

7 Conflict of interest

The authors declare no conflict of interest.

References

1. Novoselov, K. S. *et al.* Electric field effect in atomically thin carbon films. *science* **306**, 666–669 (2004).
2. Wilson, J. A. & Yoffe, A. The transition metal dichalcogenides discussion and interpretation of the observed optical, electrical and structural properties. *Advances in Physics* **18**, 193–335 (1969).
3. Wu, S. *et al.* Vapor–solid growth of high optical quality MoS₂ monolayers with near-unity valley polarization. *ACS nano* **7**, 2768–2772 (2013).
4. Peimyoo, N. *et al.* Thermal conductivity determination of suspended mono- and bilayer WS₂ by Raman spectroscopy. *Nano Research* **8**, 1210–1221 (2015).
5. Li, Y. *et al.* Enhancement of exciton emission from multilayer MoS₂ at high temperatures: intervalley transfer versus interlayer decoupling. *Small* **13**, 1700157 (2017).
6. Splendiani, A. *et al.* Emerging photoluminescence in monolayer MoS₂. *Nano letters* **10**, 1271–1275 (2010).
7. Li, Y. *et al.* Accurate identification of layer number for few-layer WS₂ and WSe₂ via spectroscopic study. *Nanotechnology* **29**, 124001 (2018).
8. Raja, A. *et al.* Coulomb engineering of the bandgap and excitons in two-dimensional materials. *Nature communications* **8**, 1–7 (2017).
9. Gong, Y. *et al.* Band gap engineering and layer-by-layer mapping of selenium-doped molybdenum disulfide. *Nano letters* **14**, 442–449 (2014).
10. Conley, H. J. *et al.* Bandgap engineering of strained monolayer and bilayer MoS₂. *Nano letters* **13**, 3626–3630 (2013).
11. Frisenda, R. *et al.* Biaxial strain tuning of the optical properties of single-layer transition metal dichalcogenides. *npj 2D Materials and Applications* **1**, 1–7 (2017).
12. Li, Z. *et al.* Active light control of the MoS₂ monolayer exciton binding energy. *ACS nano* **9**, 10158–10164 (2015).
13. Nguyen, P. V. *et al.* Visualizing electrostatic gating effects in two-dimensional heterostructures. *Nature* **572**, 220–223 (2019).
14. Fernández, L. *et al.* Renormalization of the band gap in 2D materials through the competition between electromagnetic and four-fermion interactions in large N expansion. *Physical Review D* **102**, 016020 (2020).
15. Chaves, A. *et al.* Bandgap engineering of two-dimensional semiconductor materials. *npj 2D Materials and Applications* **4**, 1–21 (2020).

16. Tonndorf, P. *et al.* Photoluminescence emission and Raman response of monolayer MoS₂, MoSe₂, and WSe₂. *Optics express* **21**, 4908–4916 (2013).
17. Zhou, C. *et al.* Self-driven WSe₂ photodetectors enabled with asymmetrical van der Waals contact interfaces. *npj 2D Materials and Applications* **4**, 1–9 (2020).
18. Xiao, J., Zhao, M., Wang, Y. & Zhang, X. Excitons in atomically thin 2D semiconductors and their applications. *Nanophotonics* **6**, 1309–1328 (2017).
19. Liu, W. *et al.* Strong exciton–plasmon coupling in MoS₂ coupled with plasmonic lattice. *Nano letters* **16**, 1262–1269 (2016).
20. Ross, J. S. *et al.* Electrically tunable excitonic light-emitting diodes based on monolayer WSe₂ p–n junctions. *Nature nanotechnology* **9**, 268–272 (2014).
21. Castellanos-Gomez, A. *et al.* Deterministic transfer of two-dimensional materials by all-dry viscoelastic stamping. *2D Materials* **1**, 011002 (2014).
22. Kunstmann, J. *et al.* Momentum-space indirect interlayer excitons in transition-metal dichalcogenide van der Waals heterostructures. *Nature Physics* **14**, 801–805 (2018).
23. Ding, L. *et al.* Understanding interlayer coupling in TMD-HBN heterostructure by Raman spectroscopy. *IEEE Transactions on Electron Devices* **65**, 4059–4067 (2018).
24. Rojas-Lopez, R. R. *et al.* Photoluminescence and charge transfer in the prototypical 2D/3D semiconductor heterostructure MoS₂/GaAs. *Applied Physics Letters* **119**, 233101 (2021).
25. Purdie, D. *et al.* Cleaning interfaces in layered materials heterostructures. *Nature communications* **9**, 1–12 (2018).
26. Haigh, S. J. *et al.* Cross-sectional imaging of individual layers and buried interfaces of graphene-based heterostructures and superlattices. *Nature materials* **11**, 764–767 (2012).
27. Tyurnina, A. V. *et al.* Strained bubbles in van der Waals heterostructures as local emitters of photoluminescence with adjustable wavelength. *ACS photonics* **6**, 516–524 (2019).
28. Hwang, Y., Kim, T. & Shin, N. Interlayer Energy Transfer and Photoluminescence Quenching in MoSe₂/Graphene van der Waals Heterostructures for Optoelectronic Devices. *ACS Applied Nano Materials* **4**, 12034–12042 (2021).
29. Huang, J., Hoang, T. B. & Mikkelsen, M. H. Probing the origin of excitonic states in monolayer WSe₂. *Scientific reports* **6**, 1–7 (2016).
30. Liu, E. *et al.* Valley-selective chiral phonon replicas of dark excitons and trions in monolayer WSe₂. *Physical Review Research* **1**, 032007 (2019).
31. He, M. *et al.* Valley phonons and exciton complexes in a monolayer semiconductor. *Nature communications* **11**, 1–7 (2020).
32. Li, Z., Wang, T., Miao, S., Lian, Z. & Shi, S.-F. Fine structures of valley-polarized excitonic states in monolayer transitional metal dichalcogenides. *Nanophotonics* **9**, 1811–1829 (2020).
33. Wu, Z. *et al.* Defects as a factor limiting carrier mobility in WSe₂: A spectroscopic investigation. *Nano Research* **9**, 3622–3631 (2016).
34. Wu, Z. & Ni, Z. Spectroscopic investigation of defects in two-dimensional materials. *Nanophotonics* **6**, 1219–1237 (2017).
35. Luo, X. *et al.* Effects of lower symmetry and dimensionality on Raman spectra in two-dimensional WSe₂. *Physical Review B* **88**, 195313 (2013).
36. Zhao, W. *et al.* Lattice dynamics in mono- and few-layer sheets of WS₂ and WSe₂. *Nanoscale* **5**, 9677–9683 (2013).
37. Terrones, H. *et al.* New first order Raman-active modes in few layered transition metal dichalcogenides. *Scientific reports* **4**, 1–9 (2014).
38. Del Corro, E. *et al.* Excited excitonic states in 1L, 2L, 3L, and bulk WSe₂ observed by resonant Raman spectroscopy. *Acs Nano* **8**, 9629–9635 (2014).
39. Dadgar, A. *et al.* Strain engineering and Raman spectroscopy of monolayer transition metal dichalcogenides. *Chemistry of Materials* **30**, 5148–5155 (2018).
40. Desai, S. B. *et al.* Strain-induced indirect to direct bandgap transition in multilayer WSe₂. *Nano letters* **14**, 4592–4597 (2014).
41. Melitz, W., Shen, J., Kummel, A. C. & Lee, S. Kelvin probe force microscopy and its application. *Surface science reports* **66**, 1–27 (2011).

42. Giusca, C. E. *et al.* Water affinity to epitaxial graphene: the impact of layer thickness. *Advanced Materials Interfaces* **2**, 1500252 (2015).
43. Jacobs, H., Leuchtman, P., Homan, O. & Stemmer, A. Resolution and contrast in Kelvin probe force microscopy. *Journal of applied physics* **84**, 1168–1173 (1998).
44. Barbet, S. *et al.* Cross-talk artefacts in Kelvin probe force microscopy imaging: a comprehensive study. *Journal of Applied Physics* **115**, 144313 (2014).
45. Jacobs, H., Knapp, H. & Stemmer, A. Practical aspects of Kelvin probe force microscopy. *Review of scientific instruments* **70**, 1756–1760 (1999).
46. Castanon, E. G. *et al.* Calibrated Kelvin-probe force microscopy of 2D materials using Pt-coated probes. *Journal of Physics Communications* **4**, 095025 (2020).
47. Matković, A. *et al.* Interfacial band engineering of MoS₂/gold interfaces using pyrimidine-containing self-assembled monolayers: toward contact-resistance-free bottom-contacts. *Advanced Electronic Materials* **6**, 2000110 (2020).
48. Xiao, J., Zhang, Y., Chen, H., Xu, N. & Deng, S. Enhanced performance of a monolayer MoS₂/WSe₂ heterojunction as a photoelectrochemical cathode. *Nano-Micro Letters* **10**, 1–9 (2018).
49. Liu, W., Cao, W., Kang, J. & Banerjee, K. High-performance field-effect-transistors on monolayer-WSe₂. *ECS Transactions* **58**, 281 (2013).

Supplementary information: Exciton tuning in monolayer WSe₂ via substrate induced electron doping

Yang Pan^{1,2*}, Mahfujur Rahaman³, Lu He^{1,2}, Ilya Milekhin^{1,2}, Gopinath Manoharan⁴, Muhammad Awais Aslam⁵, Thomas Blaudeck^{2,4,6}, Andreas Willert⁶, Aleksandar Matković⁵, Teresa I. Madeira^{1,2}, and Dietrich R. T. Zahn^{1,2}

¹Semiconductor Physics, Institute of Physics, Chemnitz University of Technology, Chemnitz, Germany

²Center for Materials, Architectures, and Integration of Nanomembranes (MAIN), Chemnitz University of Technology, Chemnitz, Germany

³Department of Electrical and Systems Engineering, University of Pennsylvania, Philadelphia, PA, USA

⁴Center for Microtechnologies, Chemnitz University of Technology, Chemnitz, Germany

⁵Institute of Physics, Montanuniversität Leoben, Leoben, Austria

⁶Fraunhofer Institute for Electronic Nano Systems, Chemnitz, Germany

*Corresponding author: yang.pan@physik.tu-chemnitz.de

1 Sample preparation

1.1 WSe₂/hBN/HOPG hetero-stack

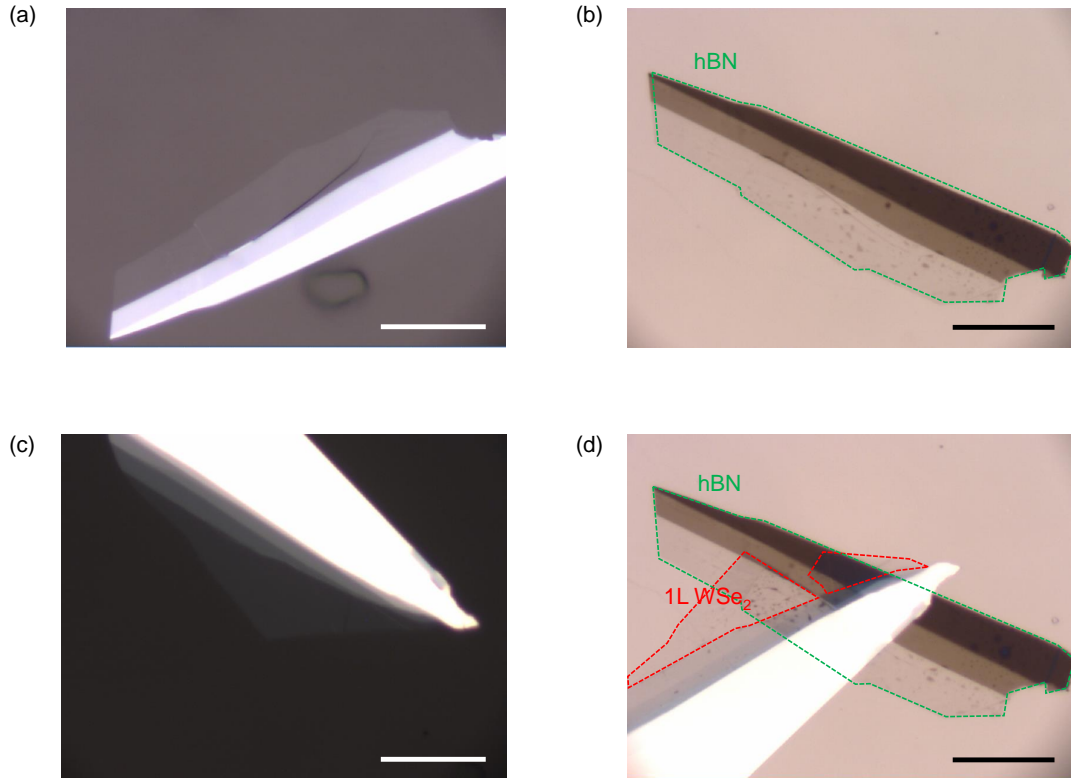


Figure 1S: Optical microscope images of few layer hBN on (a) PDMS, (b) HOPG and monolayer WSe₂ on (c) PDMS, (d) hBN/HOPG. Scale bar in figure is 20 μm.

Monolayer WSe₂ and few layer hBN are mechanical exfoliated from their bulk materials via Nitto tape on PDMS stamp (as shown in Fig. 1S (a) and (c)). WSe₂ is firstly characterized by PL and Raman spectroscopy to identify the layer numbers before transfer. After confirming the layer numbers, the HOPG top layer is cleaved to ensure a clean surface. The hBN and WSe₂ are immediately transferred bottom-to-top with a all-dry deterministic transfer technique[1].

1.2 WSe₂/graphene/hBN/HOPG hetero-stack

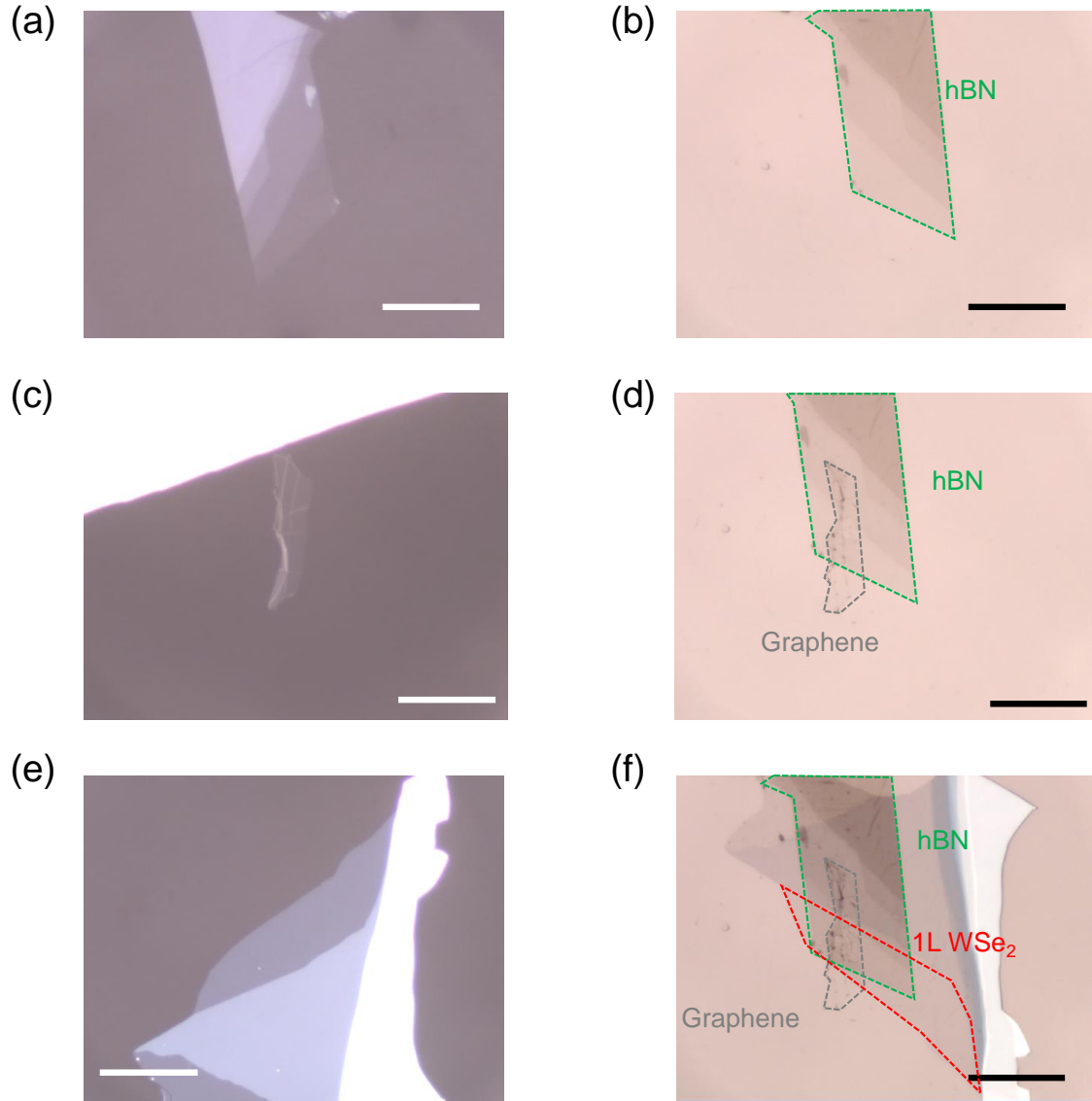


Figure 2S: Optical microscope images of few layer hBN on (a) PDMS, (b) HOPG, graphene on (c) PDMS, (d) hBN/HOPG and monolayer WSe₂ on (e) PDMS, (f) graphene/hBN/HOPG. Scale bar in figure is 20 μm.

The sample preparation procedure is same as mentioned above.

2 Stokes shift of monolayer WSe₂

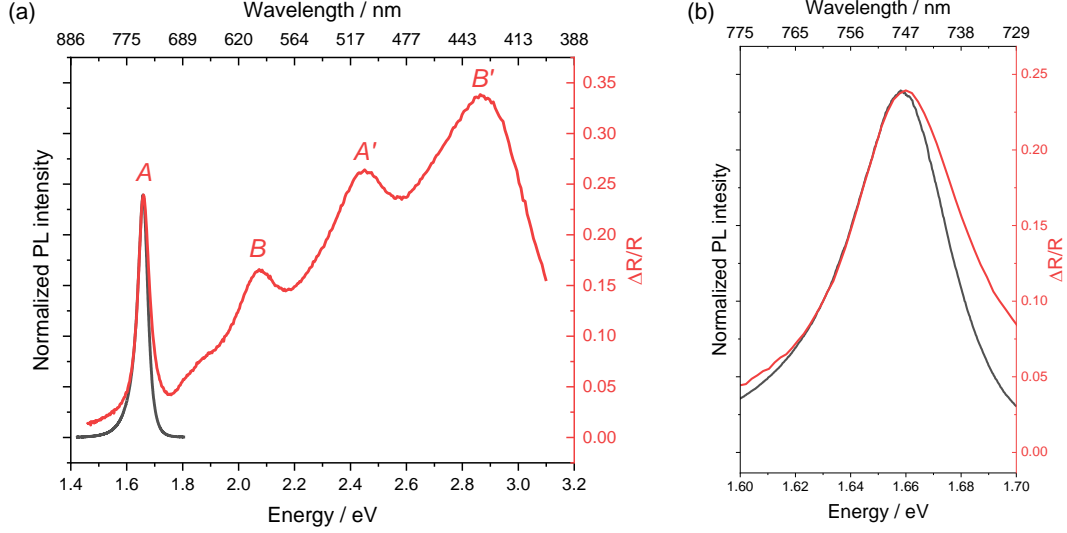


Figure 3S: (a) Micro PL and micro reflectance contrast spectra of monolayer WSe₂. (b) zoomed in for 1.60-1.70 eV.

Micro reflectance contrast measurements are carried out with a Zeiss AxioImager.M2m microscope in epi-illumination configuration equipped with a 50x, 0.75NA objective, a Zeiss HAL 100 illuminator-12 V/ 100W white-light source with intensity control and coupled to a J&M Analytik AG Tidas S MSP 800 spectrometer operable in the spectral range 200-980 nm [2, 3].

For the ultra-thin film on a transparent substrates, $\Delta R/R$ is predominantly determined by the imaginary part of the dielectric function, which is proportional to the optical absorption[4–7].

We measured the micro PL and micro reflectance contrast spectra to extract the Stokes shift of monolayer WSe₂ to make sure that it is reasonable to consider the PL peak energy position corresponding to the exciton energy. As shown in Fig. 3S, we only observe a ~ 2 meV Stokes shift, which makes it fair enough to consider the exciton PL peak position as the exciton energy.

3 AFM and KPFM

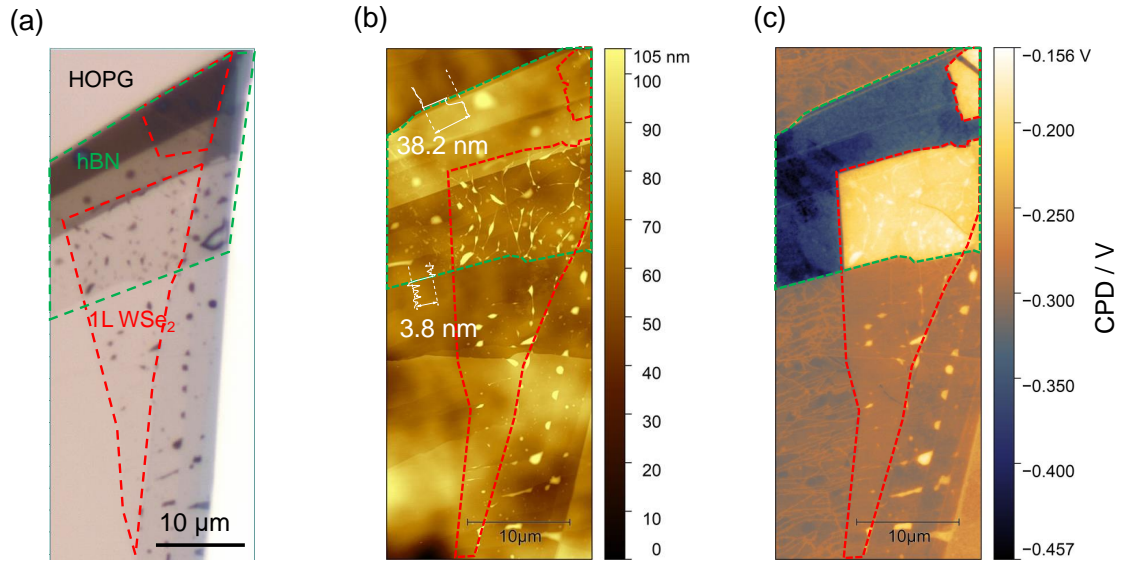


Figure 4S: (a) optical microscope image, (b) AFM height image, and (c) KPFM image of WSe₂/hBN/HOPG hetero-stack.

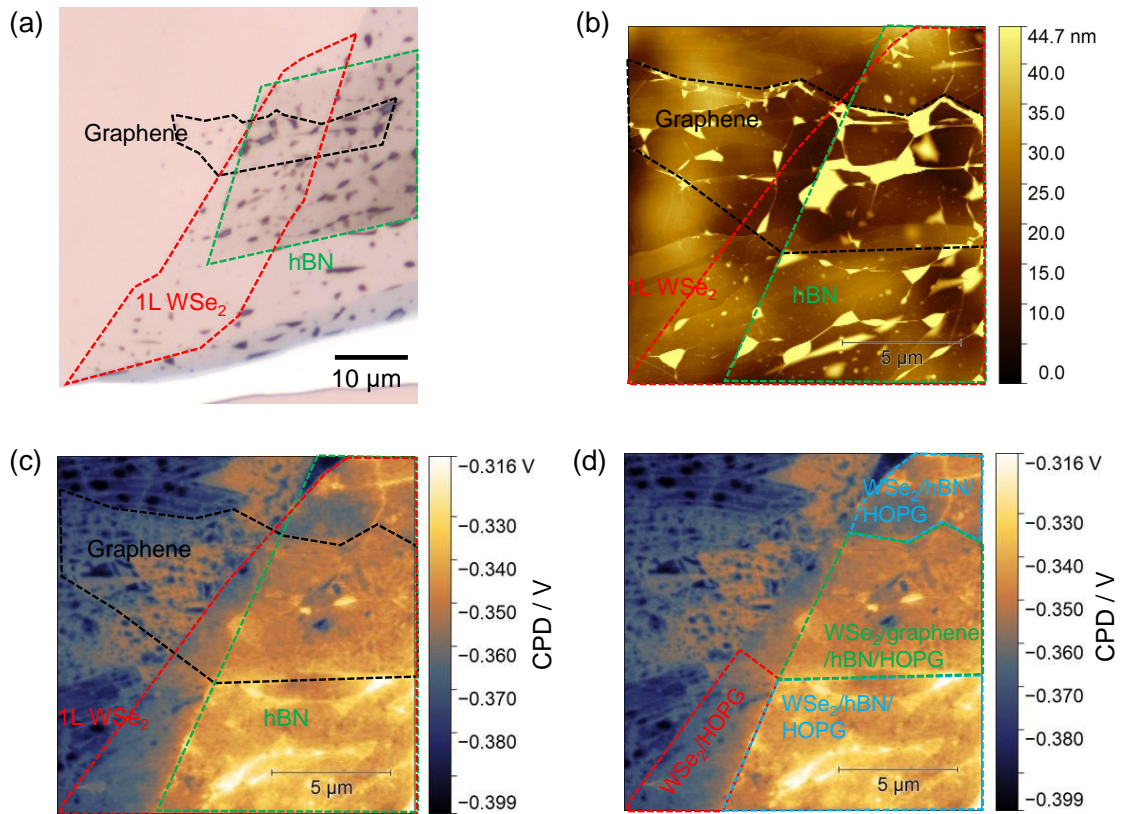


Figure 5S: (a) optical microscope image, (b) AFM height image, and (c-d) KPFM image of WSe₂/graphene/hBN/HOPG hetero-stack.

4 Work function determination of HOPG

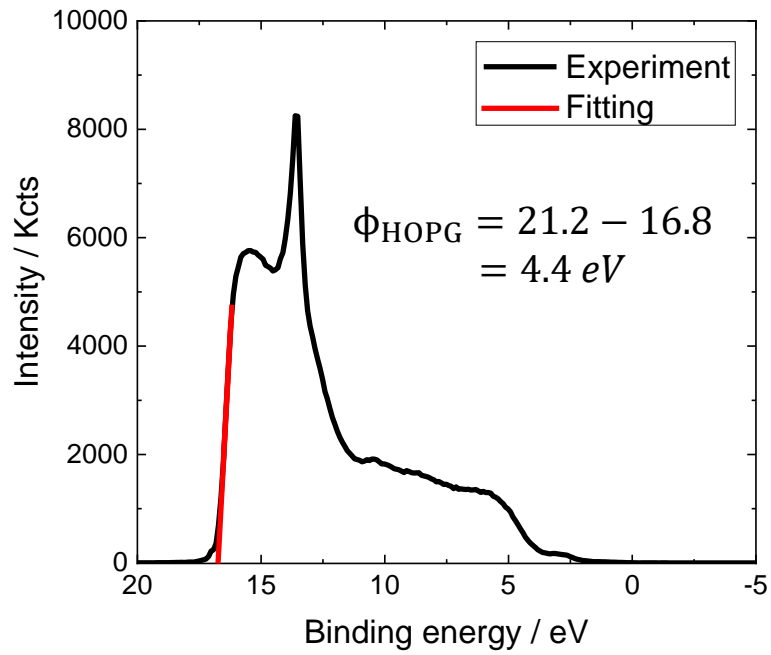


Figure 6S: UPS spectra of HOPG.

We use ultraviolet photoelectron spectroscopy (UPS) to determine the absolute work function of HOPG [8]. The He-I light source has an energy of 21.2 eV and the secondary electron cutoff (SEC) is 16.8 eV. The work function of HOPG is 4.4 eV.

References

1. Castellanos-Gomez, A. *et al.* Deterministic transfer of two-dimensional materials by all-dry viscoelastic stamping. *2D Materials* **1**, 011002 (2014).
2. Sowade, E., Blaudeck, T. & Baumann, R. R. Self-assembly of spherical colloidal photonic crystals inside inkjet-printed droplets. *Crystal Growth & Design* **16**, 1017–1026 (2016).
3. Kuhn, E. *et al.* Disorder explains dual-band reflection spectrum in spherical colloidal photonic supraparticle assemblies. *Nano Select* **2**, 2461–2472 (2021).
4. Raja, A. *et al.* Coulomb engineering of the bandgap and excitons in two-dimensional materials. *Nature communications* **8**, 1–7 (2017).
5. Li, Y. *et al.* Measurement of the optical dielectric function of monolayer transition-metal dichalcogenides: MoS₂, MoSe₂, WS₂, and WSe₂. *Physical Review B* **90**, 205422 (2014).
6. Zhao, W. *et al.* Evolution of electronic structure in atomically thin sheets of WS₂ and WSe₂. *ACS nano* **7**, 791–797 (2013).
7. McIntyre, J. & Aspnes, D. E. Differential reflection spectroscopy of very thin surface films. *Surface Science* **24**, 417–434 (1971).
8. Kim, J. W. & Kim, A. Absolute work function measurement by using photoelectron spectroscopy. *Current Applied Physics* **31**, 52–59 (2021).